Electronic Supplementary Material (ESI) for Dalton Transactions.

Supplemental Data

Triply Bridged Dinuclear Ruthenium Complexes Bearing Alkylbis(2-pyridylmethyl)amine in the Mixed-Valence State of Ru(II)-Ru(III)

Tomoyo Misawa-Suzuki, Kazuhiro Matsuya, Takashi Watanabe and Hirotaka Nagao*

Department of Materials and Life Sciences, Sophia University

7-1 Kioicho, Chiyodaku, Tokyo 102-8554 Japan

I. Electron Spin Resonance (ESR) spectra

X-band ESR spectra for (**a**) $[\mathbf{1}]^{2+}$, (**b**) $[\mathbf{2}]^{2+}$, (**c**) $[\mathbf{3}]^{2+}$, (**d**) $[\mathbf{4}]^{2+}$ and (**e**) $[\mathbf{6}]^{2+}$, as shown in Fig. S1, were recorded with a JEOL JESFA300 ESR spectrometer at 77 K in frozen acetone. An unpaired electronic spin on the $\{Ru_2(\mu\text{-}X)(\mu\text{-}Y)(\mu\text{-}Z)\}$ core was ensured.

When an electronic spin was on the Ru center, the *g*-value should have a significant anisotropy because of the spin-orbit coupling interaction of the Ru ions. Actually, the principle values of g_1, g_2 and g_3 were reported to be 2.2 - 1.9 in our case. On the other hand, the *g*-value is isotropic with its value of 2.00 in the case with an organic radical.

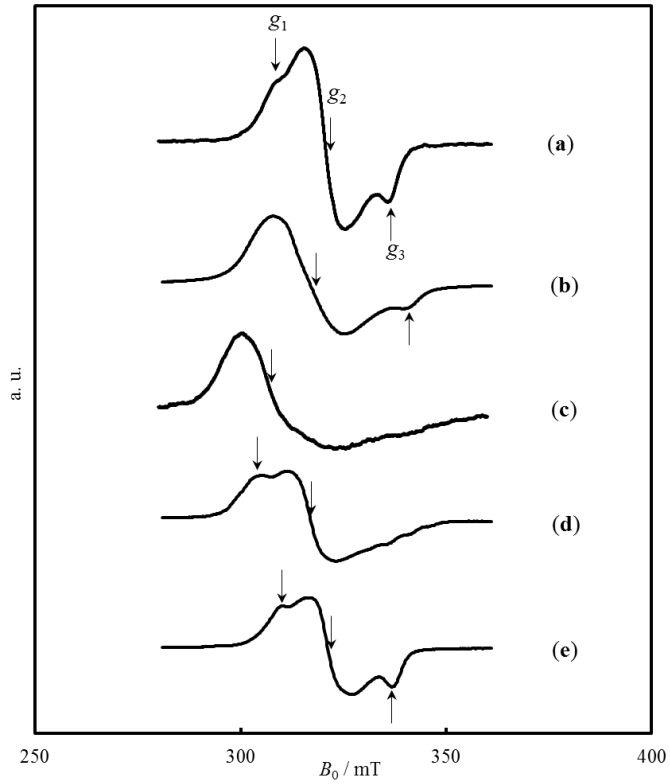

Fig. S1 X-band ESR spectra in frozen acetone at 77 K

Table S1 *g*-values of ESR signals

Ru(II)-Ru(III) Complexes	g_1	g_2	g_3	Frequency / MHz	Power / mW	Mod. width / mT	Amplitude	Sweep time / min.	Time const. / s
$[\mathbf{1}]^{2+}$	2.11	2.03	1.94	9118.38	0.998	0.6	14	4	0.1
$[\mathbf{2}]^{2+}$	-	2.07	1.93	9114.96	0.998	0.6	500	4	0.3
$[\mathbf{3}]^{2+}$	-	2.10	-	9156.05	0.998	2.0	500	4	0.3
$[\mathbf{4}]^{2+}$	2.14	2.06	-	9156.05	0.998	2.0	14	4	0.1
$[\mathbf{6}]^{2+}$	2.11	2.03	1.94	9157.03	0.995	2.0	20	4	0.1

II. NMR spectra

^{1}H NMR and ^{13}C NMR of bendylbis(2-pyridyl)methylamine (bbpma) were measured in CD_2Cl_2 at room temperature with JEOL AL400 spectrometer.

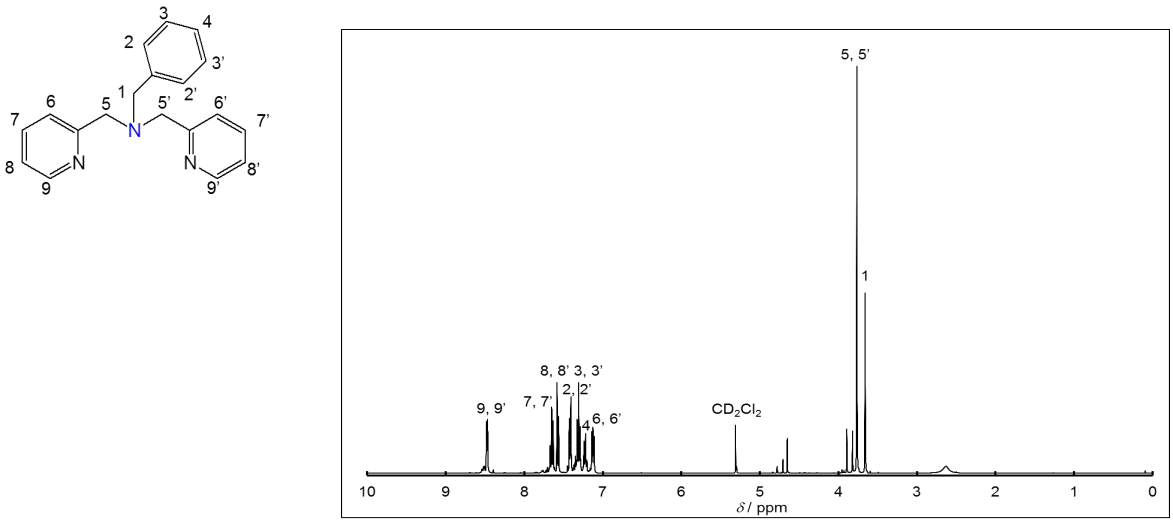

Fig. S2 ^{1}H NMR of bbpma in CD_2Cl_2

Chemical shift / ppm (position, multiplicity, coupling constant / Hz); 3.66 (1, s), 3.76 (5, 5', s), 7.13 (6, 6', m), 7.22 (m) 7.31 (3. 3', t, J = 7.63), 7.42 (2, 2', d, J = 7.02), 7.57 (8, 8', d, J = 7.93), 7.65 (7, 7', td, J = 6.87), 8.48 (9, 9', d, J = 6.41).

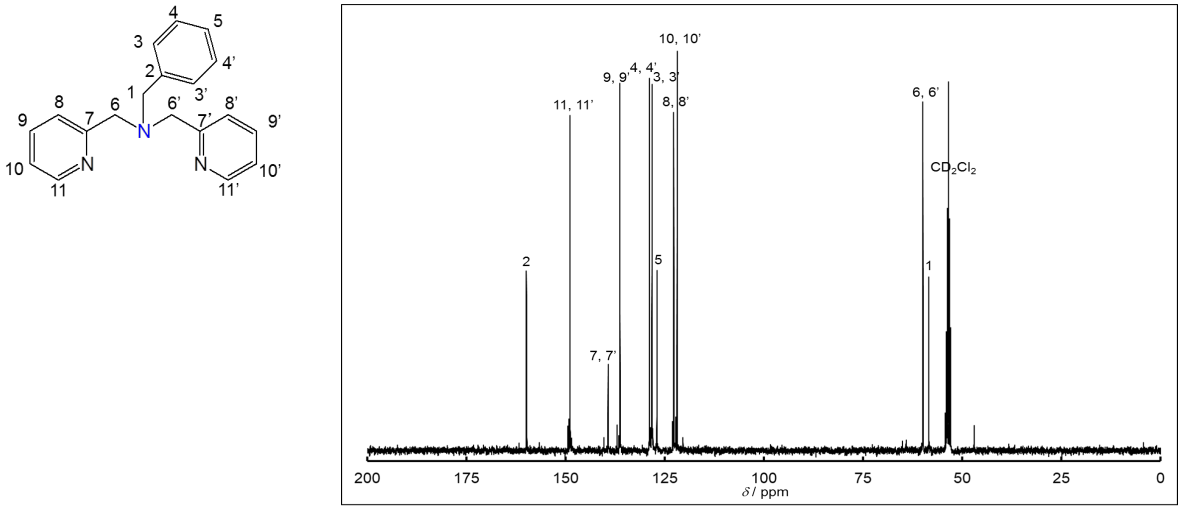

Fig. S3 ^{13}C NMR of bbpma in CD_2Cl_2

Chemical shift / ppm (position); δ 58.76 (1), 60.23 (6, 6') 122.22 (10, 10'), 123.07 (8, 8'), 127.31 (5), 128.56 (3, 3'), 129.20 (4, 4'), 136.63 (9, 9'), 139.63 (7, 7'), 149.23 (11, 11'), 160.22 (2).

III. Single crystal X-ray structural analysis

Single crystals of [**2**]$(PF_6)_2\cdot(CH_3)_2CO$, [**3**]$(PF_6)_2\cdot 0.5H_2O\cdot(CH_3)_2CO$, [**4**]$(PF_6)_2\cdot H_2O$ were obtained by diffusion of diethyl ether into $(CH_3)_2CO$ solutions. The intensity data were collected on a Rigaku Mercury CCD diffractometer, using graphic monochromatized Mo*K*α radiation (0.71069 Å). All the calculations were carried out using the Crystal Structure software package. Structures were solved by a direct method, expanded using Fourier techniques and refined using full-matrix least-squares techniques.

The crystallographic data are summarized in Table S2 and structural parameters around the ruthenium center of *fac*-type mononuclear ruthenium complexes bearing ebpma, *fac*-$[Ru^{III}Cl_3(ebpma)]$, *fac*-$[Ru^{II}(NCCH_3)_3(ebpma)]^{2+}$ and *fac*-$[RuCl_2(NO)(ebpma)]^{+}$, in Table S3.

Table S2 Crystallographic data of triply bridged diruthenium complexes

	[**2**]$^{2+}$	[**3**]$^{2+}$	[**4**]$^{2+}$
X	Cl	Br	OCH_3
Y	Cl	Br	OCH_3
Z	Cl	Cl	Br
Formula	$[\{Ru(ebpma)\}_2(\mu\text{-}Cl)_3](PF_6)_2\cdot(CH_3)_2CO$	$[\{Ru(ebpma)\}_2(\mu\text{-}Cl)(\mu\text{-}Br)_2](PF_6)_2\cdot 0.5H_2O\cdot(CH_3)_2CO$	$[\{Ru(ebpma)\}_2(\mu\text{-}Br)(\mu\text{-}OMe)_2](PF_6)_2\cdot H_2O$
	$C_{29.5}H_{37}N_6OF_{12}P_2Cl_3Ru_2$	$C_{31}H_{41}N_6O_{1.5}F_{12}P_2ClBr_2Ru_2$	$C_{30}H_{42}N_6O_3F_{12}P_2Ru_2Br$
M_w	1111.12	1218.04	1106.67
Crystal dimensions / mm	0.200 x 0.160 x 0.030	0.07 x 0.07 x 0.03	0.160 x 0.100 x 0.030
Shape	platelet	platelet	platelet
Colour	Blue	Green	Green
Crystal system	Monoclinic	Orthorhombic	Orthorhombic
Space group	$P2_1/c$ (# 14)	*Pmmn* (# 59)	*Pbcn* (# 60)
a (Å)	12.428(11)	13.913(3)	12.8500(7)
b (Å)	26.83(2)	15.805(4)	18.1669(8)
c (Å)	13.129(11)	9.095(2)	16.6491(9)
α (º)	90	90	90
β (º)	118.229(4)	90	90
γ (º)	90	90	90
V (Å^3)	3857(6)	2000.0(8)	3886.6(3)
Z	4	2	4
D_{calcd} / g cm^{-3}	1.913	2.022	1.891
μ(Mo*K*α) / cm^{-1}	11.702	30.023	19.900
T / ºC	-180	-180	-180
No. of reflections	37398	15087	28530
No. of unique reflections	8797	2465	4433
R [a)]	0.0549	0.0300	0.0459
wR [b)]	0.1209	0.0702	0.1092
GOF	1.111	1.093	1.096

a) $R = \Sigma||F_o| - |F_c|| / \Sigma|F_o|$ b) $wR = [\Sigma(w(F_o^2 - F_c^2)^2) / \Sigma w(F_o^2)^2]^{1/2}$

Table S3 Comparisons of the structural parameters

	$[\mathbf{2}]^{2+}$	$[\mathbf{3}]^{2+}$	$[\mathbf{4}]^{2+}$	$[\mathbf{1}]^{2+}$ *2			
X Y Z	Cl Cl Cl	Br Br Cl	OCH_3 OCH_3 Br	OCH_3 OCH_3 Cl	$[Ru^{III}Cl_3(ebpma)]$ *1	$[Ru^{II}(AN)_3(ebpma)]^{2+}$ *1 (AN = $NCCH_3$)	$[RuCl_2(NO)(ebpma)]^+$ *1
Ru-N(amine) / Å	2.107(4) 2.116(5)	2.119(4),	2.112(3)	2.109(2)	2.134(3)	2.127(2)	2.137(3)
Ru-N(py, *trans*-X / Å	2.057(5)	2.5216(5)	2.064(3)	2.062(2)	2.066(3) 2.092(3)	2.064(2), 2.056(2)	2.090(3), 2.103(3)
Ru-N (py, *trans*-Y)/ Å	2.047(3)	2.5216(5)	2.070(3)	2.055(2)			
N(amine)-Ru -N(py) / °	82.99(14) 79.54(18) 83.74(16) 79.82(16)	82.63(10)	82.14(12) 82.53(13)	82.80(11) 82.45(10)	81.41(13), 78.57(13)	82.72(13), 82.17(12)	82.23(13), 80.99(12)
N(py)-Ru -N(py) / °	90.66(17) 86.04(16)	88.44(9)	84.78(12)	84.86(10)	92.62(12)	83.88(12)	82.58(13)

*1) Y. Shimizu, S. Fukui, T. Oi and H. Nagao, *Bull. Chem. Soc. Jpn.*, **2008**, *81*, 1285.

*2) K. Matsuya, S. Fukui, Y. Hoshino and H. Nagao, *Dalton Trans.*, **2009**, 7876.

IV. Electrochemical behaviors in CH_3CN

Cyclic voltammograms of the triply bridged dinuclear ruthenium complexes (1.0 mmol dm^{-3}) were measured in CH_3CN containing 0.1 mol dm^{-3} TEAP at room temperature using a Pt working electrode, a Pt counter electrode, and a reference electrode of Ag | 0.01 mol dm^{-3} $AgNO_3$ (CH_3CN) (Fig. 4, Table 2).

Hydrodynamic voltammetry (HDV) were carried out using a BAS RDE-2 analyzer by a rotating platinum working disk electrode (ϕ = 3.0 mm). The plots of limiting current i_d *vs*. square root of rotating rate of the working electrode $\omega^{1/2}$ was made and the electrode reactions was revealed to be diffusion limiting reactions, according to the Levich equation* and the ln-plots *vs*. *E* were made based on the Nernst equation** to calcualte the number of electrons involved in the redox processes. Normal pulse voltammetry (NPV) was used to analyze the redox waves according to the Cottrell equation.*** Hydrodynamic voltammograms, ln-plots and normal pulse voltammograms are summarized in Figs. S4 - S7, Tables S2 and S3.

* Levich equation; $i_d = 0.620nFAD^{2/3}\omega^{1/2}v^{1/6}c$ (i_d: limiting current, A: the electrode area, ω: the angular rotation rate of the electrode, D: diffusion coefficient, v: the viscosity, c: concentration of the sample)

**Nernst equation; $E = E_{1/2} + \frac{RT}{nF}\ln\frac{i}{i_d - i}$ (n: the number of electrons, F: Faraday constant)

***Cottrell equation; $i_d = \frac{nFD^{1/2}c}{\pi^{1/2}t^{1/2}} (\omega^{1/2} = t^{-1/2})$

All these complexes showed two reversible one-electron oxidation eq. (S1) and reduction eq. (S2) processes.

$$\text{Ru(II)-Ru(III)} \rightleftarrows \text{Ru(III)-Ru(III)} + e^- \quad \text{(S1)}$$

$$\text{Ru(II)-Ru(III)} + e^- \rightleftarrows \text{Ru(II)-Ru(II)} \quad \text{(S2)}$$

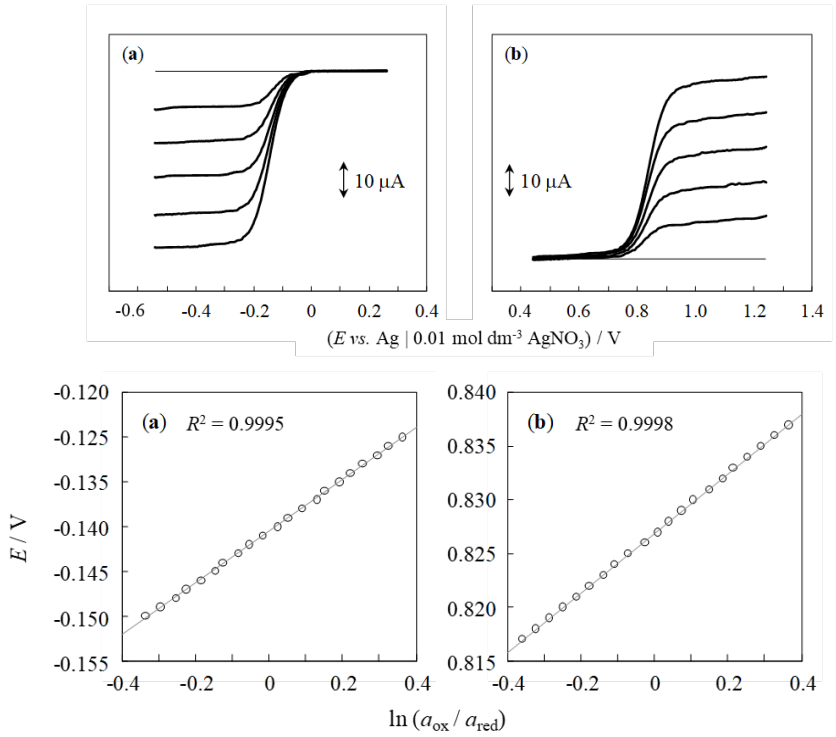

Fig. S4 Hydrodynamic voltammograms and analyses of the redox waves of [**2**]$(PF_6)_2$ in CH_3CN (100, 400, 900, 1600, 2500 rpm, (**a**) reduction wave, (**b**) oxidation wave)

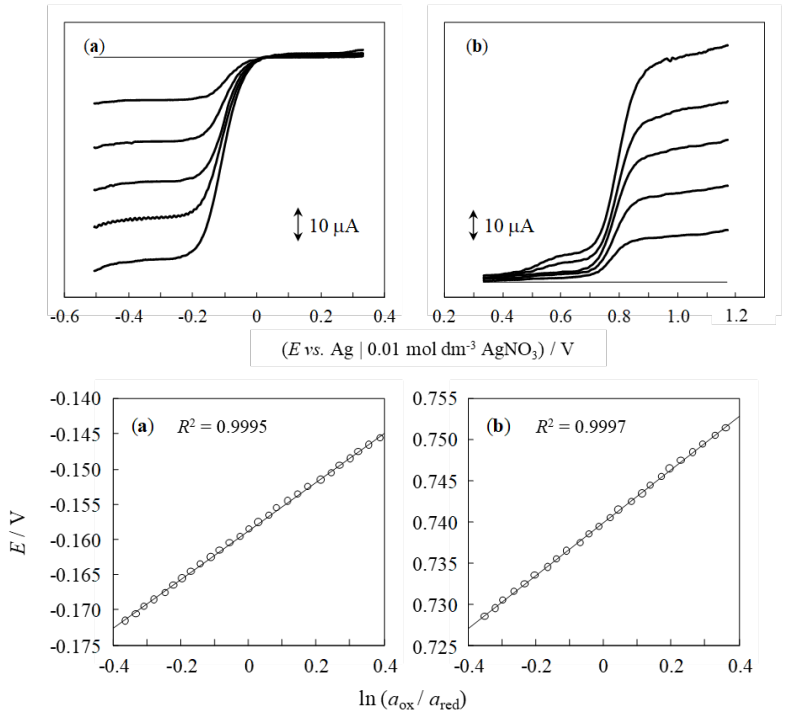

Fig. S5 Hydrodynamic voltammograms and analyses of the redox waves of [**3**]$(PF_6)_2$ in CH_3CN (100, 400, 900, 1600, 2500 rpm, (**a**) reduction wave, (**b**) oxidation wave)

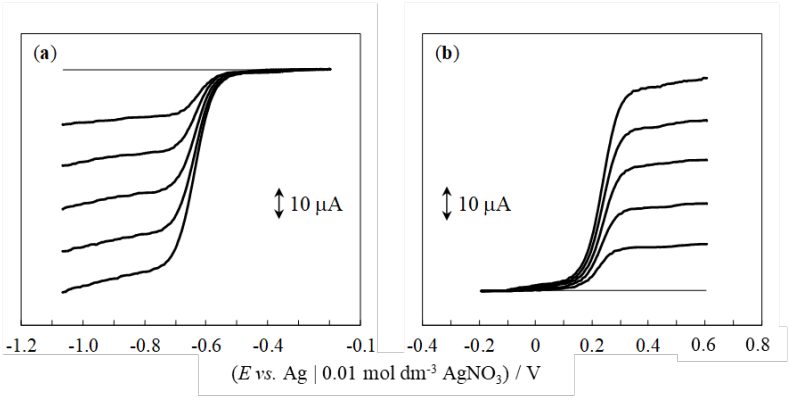

Fig. S6 Hydrodynamic voltammograms of the redox waves of [**4**]$(PF_6)_2$ in CH_3CN (100, 400, 900, 1600, 2500 rpm, (**a**) reduction wave, (**b**) oxidation wave)

Table S4 Analyses of the HDVs in CH_3CN (900 rpm)

Rpm	Oxidation		reduction	
	$E_{1/2}$ / V	(RT/nF) / V	$E_{1/2}$ / V	(RT/nF) / V
100	0.215	0.0264	-0.613	0.0247
400	0.223	0.0292	-0.627	0.0284
900	0.229	0.0294	-0.628	0.0279
1600	0.228	0.0298	-0.630	0.0286
2500	0.228	0.0297	-0.631	0.0287

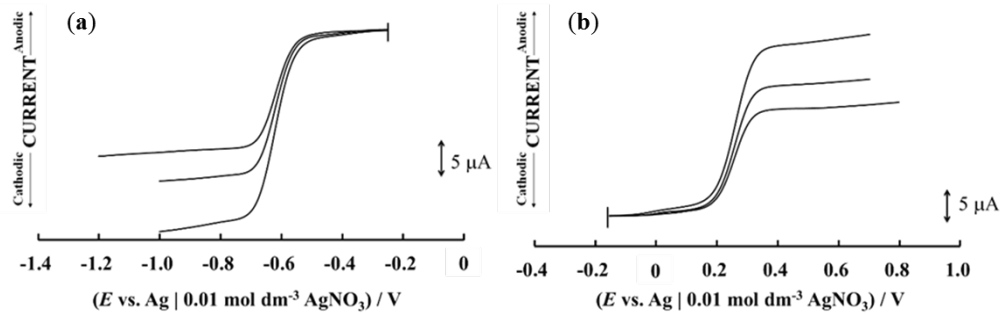

Fig. S7 NPVs of the redox waves of [**6**]$(PF_6)_2$ in CH_3CN (sampling width; 20, 60, 96 ms, (**a**) reduction wave, (**b**) oxidation wave)

Table. S5 Analyses of the NPVs in CH_3CN (900 rpm)

sampling width / ms	(**a**)			(**b**)		
	$E_{1/2}$calcd. / V	$E_{1/2}$obs. / V	(RT/nF) / V	$E_{1/2}$calcd. / V	$E_{1/2}$obs. / V	(RT/nF) / V
20	-0.61	-0.61	0.026	0.25	0.26	0.026
60	-0.60	-0.61	0.023	0.24	0.26	0.025
96	-0.60	-0.61	0.022	0.25	0.26	0.025

V. Spectroscopic properties in CH_2Cl_2

UV-vis-NIR spectra were obtained in CH_2Cl_2 at room temperature using a quartz cell of 1 cm path length. For all the complexes, in common, in the UV-vis region, two intense absorption bands, which were assigned to π-π* transition and MLCT band (dπ(Ru)-π*(ebpma)) respectively, and two kinds of weak broad bands in the NIR region were observed: one intense and broad band around 700 - 800 nm and a weaker broad band around 1500 nm, which were attributed to the inter-valence (IVCT) band.

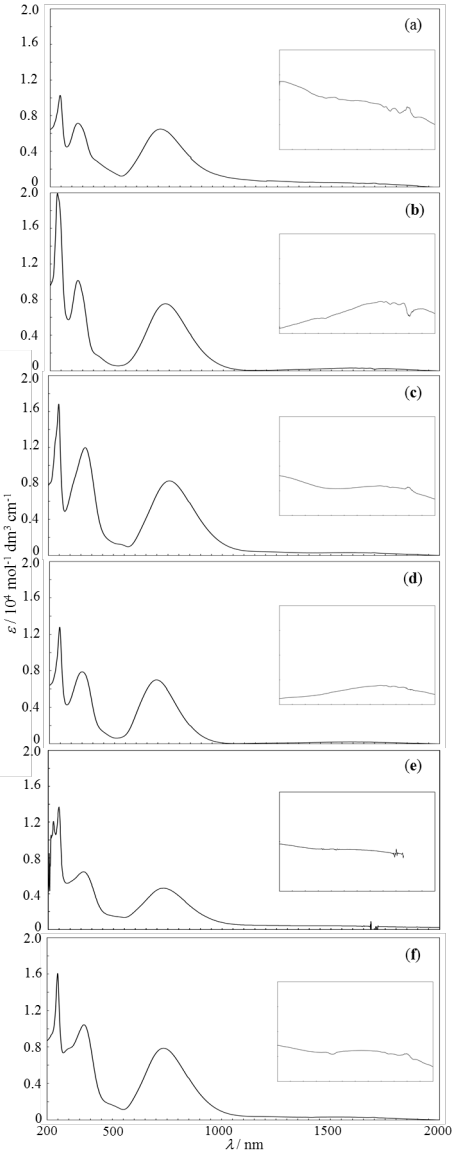

Fig. S8 UV-vis-NIR spectra of the Ru(II)-Ru(III) complexes in CH_2Cl_2; (**a**) [**2**]$(PF_6)_2$, (**b**) [**3**]$(PF_6)_2$, (**c**) [**4**]$(PF_6)_2$, (**d**) [**5**]$(PF_6)_2$, (**e**) [**6**]$(PF_6)_2$ and (**f**) [**1**]$(PF_6)_2$ [*2]

The λ_{max} values for [**2**]$(PF_6)_2$ were independent of the kind of solvent or polarity of measurement mediator, as well as those of the reported complex, [**1**]$(PF_6)_2$ (Table S5).

Table S6 Spectroscopic properties in CH_2Cl_2

Complex	λ_{max} / nm (ε / M^{-1} cm^{-1})
[**2**]$(PF_6)_2$	328 (7150), 709 (6500), ~1500 (~500)
[**3**]$(PF_6)_2$	328 (10200), 732 (7540), ~1590 (~300)
[**4**]$(PF_6)_2$	370 (12000), 757 (8280), ~1590 (~300)
[**5**]$(PF_6)_2$	351 (7890), 693 (7000), ~1590 (~200)
[**6**]$(PF_6)_2$	362 (6500), 732 (4600), ~1530 (~410)
[**1**]$(PF_6)_2$ [*2]	370 (14000), 734 (7870), ~1520 (~300)

Table S7 Spectroscopic data of triply bridged complexes in organic solvents

	λ_{max} / nm (ε / M^{-1} cm^{-1})			
	$[\mathbf{2}]^{2+}$	$[\mathbf{3}]^{2+}$	$[\mathbf{4}]^{2+}$	$[\mathbf{1}]^{2+}$ [*2]
X	Cl	Br	OCH_3	OCH_3
Y	Cl	Br	OCH_3	OCH_3
Z	Cl	Cl	Br	Cl
CH_2Cl_2	328 (7150), 709 (6500)	328 (10200), 732 (7540)	370 (12000), 757 (8280)	370 (14000), 734 (7870)
$(CH_3)_2CO$	332 (9940), 708 (10000)	332 (12200), 729 (9450)	371 (12100), 756 (8470)	730 (82500)
CH_3CN	245 (15200), 323 (9680), 708 (9320)	324 (17000), 734 (8280)	368 (12500), 755 (8760)	248 (14210), 370 (8990), 729 (7240)
CH_3OH	246 (7520), 327 (4540), 705 (4110)	-	-	248 (16990), 370 (11900), 731 (10220)

Spectroelectrochemical measurements using an OTTLE cell (l = 1.0 mm) in acetone were carried out for [**1**]$(PF_6)_2$ at +0.50 V for oxidation and -0.70 V for reduction, [**2**]$(PF_6)_2$ at -0.25 V for reduction, and [**3**]$(PF_6)_2$ at -0.25 V for reduction reaction. Reversible spectral changes were observed in the re-oxidation reaction after the one-electron reduction reaction.

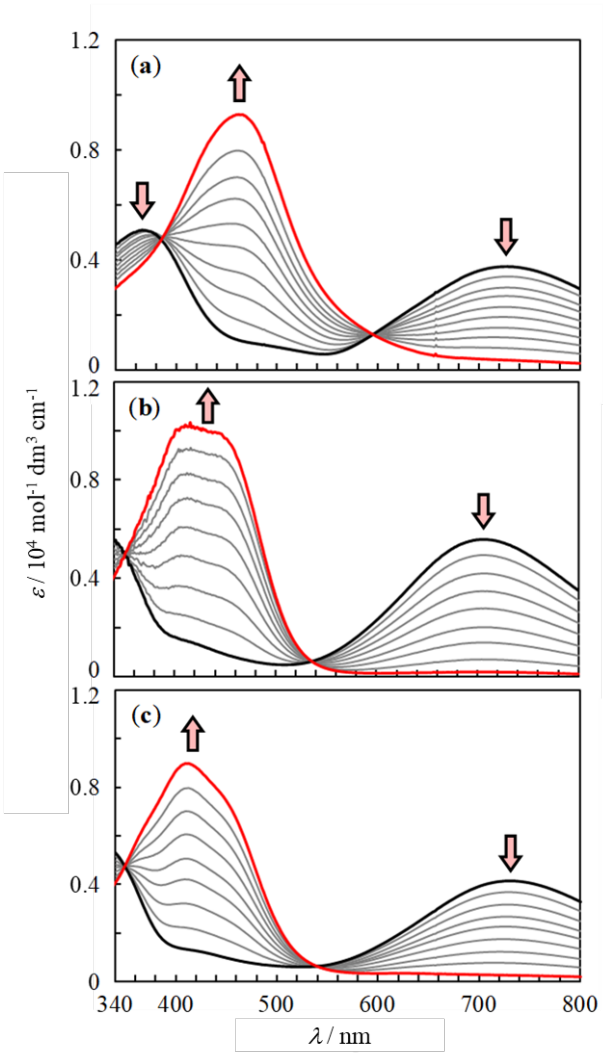

Fig. S9 Spectral changes accompanied with electrochemical one-electron reduction reactions using an OTTLE cell in $(CH_3)_2CO$ at room temperature; (**a**) $[\mathbf{1}]^{2+\,*2}$, (**b**) $[\mathbf{2}]^{2+}$, (**c**) $[\mathbf{3}]^{2+}$

VI. Density functional theory (DFT) calculations

All the calculations were performed with the Gaussian09 program.*[3] The geometry optimizations were performed at the B3LYP level of density functional theory with the SDD (Ru)-6-31++G(d,p)(C,H,O,N) basis sets. The calculated structural parameters of the $S = 1/2$ model well agreed with the experimental results as shown in Table S8.

*3) M. J. Frisch, G. W. Trucks, H. B. Schlegel, G. E. Scuseria, M. A. Robb, J. R.Cheeseman, G. Scalmani, V. Barone, B. Mennucci, G. A. Petersson, H. Nakatsuji, M. Caricato, X. Li, H. P. Hratchian, A. F. Izmaylov, J. Bloino, G. Zheng, J. L. Sonnenberg, M. Hada, M. Ehara, K. Toyota, R. Fukuda, J. Hasegawa, M. Ishida, T. Nakajima, Y. Honda, O. Kitao, H. Nakai, T. Vreven, J. A. Montgomery Jr., J. E. Peralta, F. Ogliaro, M. Bearpark, J. J. Heyd, E. Brothers, K. N. Kudin, V. N. Staroverov, R. Kobayashi, J. Normand, K. Raghavachari, A. Rendell, J. C. Burant, S. S. Iyengar, J. Tomasi, M. Cossi, N. Rega, J. M. Millam, M. Klene, J. E. Knox, J. B. Cross, V. Bakken, C. Adamo, J. Jaramillo, R. Gomperts, R. E. Stratmann, O. Yazyev, A. J. Austin, R. Cammi, C. Pomelli, J. W. Ochterski, R. L. Martin, K. Morokuma, V. G. Zakrzewski, G. A. Voth, P. Salvador, J. J. Dannenberg, S. Dapprich, A. D. Daniels, Ö. Farkas, J. B. Foresman, J. V. Ortiz, J. Cioslowski, D. J. Fox, Gaussian 09, Revision B.01, Gaussian, Inc., Wallingford CT, 2009.

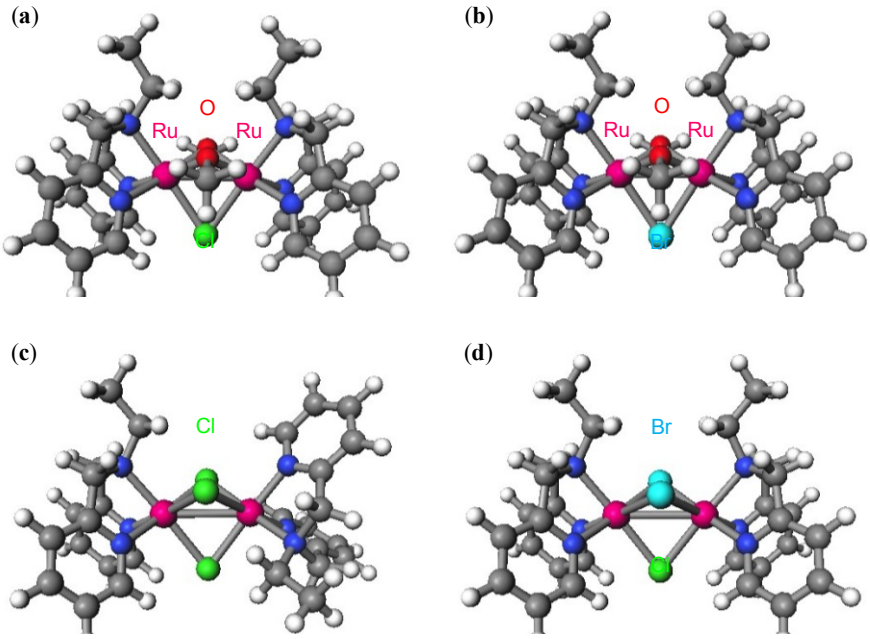

Fig. S10 Optimized structures of of the Ru(II)-Ru(III) mixed-valent complexes by DFT calculations; (**a**) $[\mathbf{1}]^{2+}$, (**b**) $[\mathbf{4}]^{2+}$, (**c**) $[\mathbf{2}]^{2+}$, (**d**) $[\mathbf{3}]^{2+}$

Table S8 Comparisons of bond distances (Å) and angles (°) between the theoretical values and experimental values

	$[\mathbf{1}]^{2+}$		$[\mathbf{4}]^{2+}$		$[\mathbf{2}]^{2+}$		$[\mathbf{3}]^{2+}$	
X Y Z	OCH_3 OCH_3 Cl		OCH_3 OCH_3 Br		Cl Cl Cl		Br Br Cl	
	Exp.	Calcd.	Exp.	Calcd.	Exp.	Calcd.	Exp.	Calcd.
Ru-Ru	2.6898(3)	2.7853	2.7072(4)	2.8066	2.8612(6)	2.9586	2.8959(3)	3.0236
Ru-N(amine)	2.109(2)	2.1540	2.113(3)	2.1606 2.1611	2.104(5) 2.105(4)	2.1605 2.1625	2.121(3)	2.1664 2.1671
Ru-N(pyridine)	2.055(2) 2.062(2)	2.0985	2.064(3) 2.070(3)	2.1065 - 2.1082	2.035(4) - 2.045(5)	2.0774 - 2.0784	2.050(2)	2.0816 - 2.0828
Ru-Cl	2.4200(9)	2.4809	—	—	2.3937(15) - 2.4108(14)	2.4602 - 2.4746	2.4120(9)	2.4719 2.4736
Ru-Br	—	—	2.5429(4)	2.6015 - 2.6017	—	—	2.5217(3)	2.5887 - 2.5912
Ru-O	2.071(2) 2.072(2)	2.1195	2.070(3) 2.068(3)	2.1079 - 2.1100	—	—	—	—
Ru-Cl-Ru	67.53(2)	68.3	—	—	72.88(3) - 73.37(3)	73.7 - 73.8	73.78(3)	75.4
Ru-Br-Ru	—	—	64.324(13)	65.3	—	—	70.087(11)	71.4 71.5
Ru-O-Ru	80.96(7)	82.6	81.71(9)	83.4	—	—	—	—
$<S^2>$		0.7569		0.7578		0.7562		0.7566

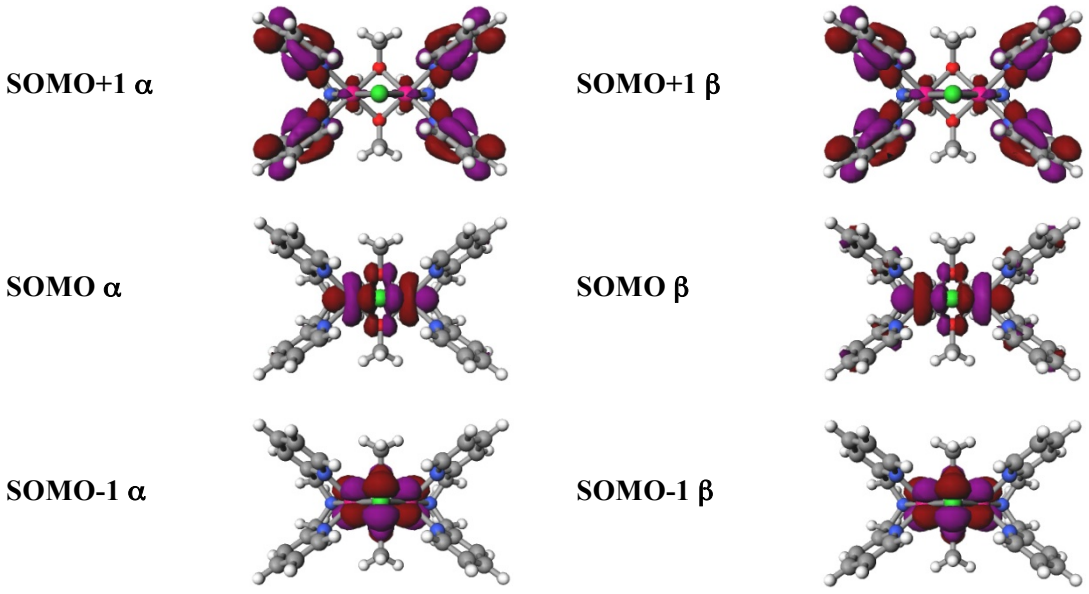

Fig. S11 Contributions to MOs from each atom of $[\mathbf{1}]^{2+}$

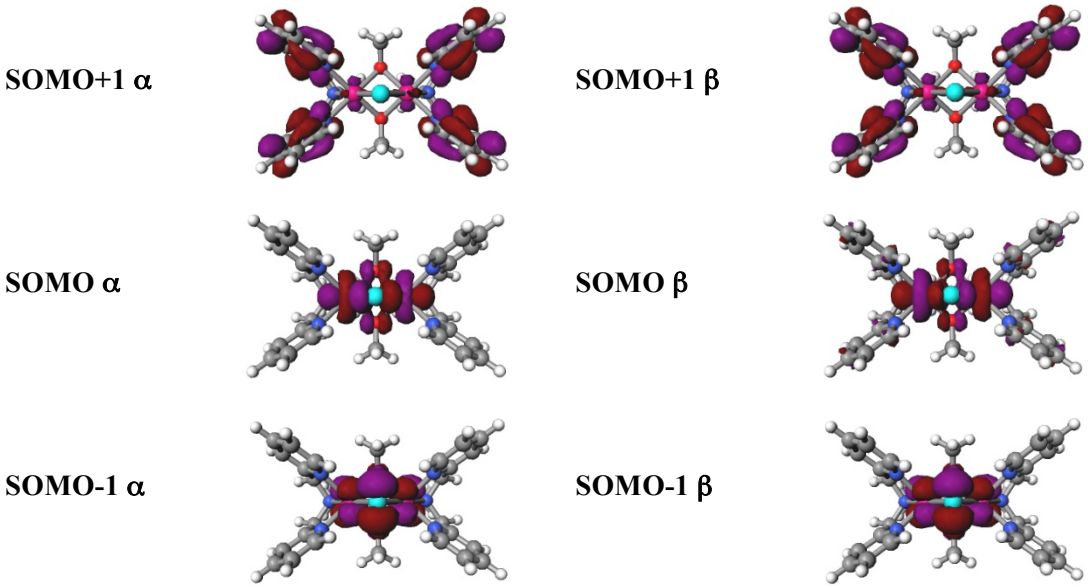

Fig. S12 Contributions to MOs from each atom of $[\mathbf{4}]^{2+}$

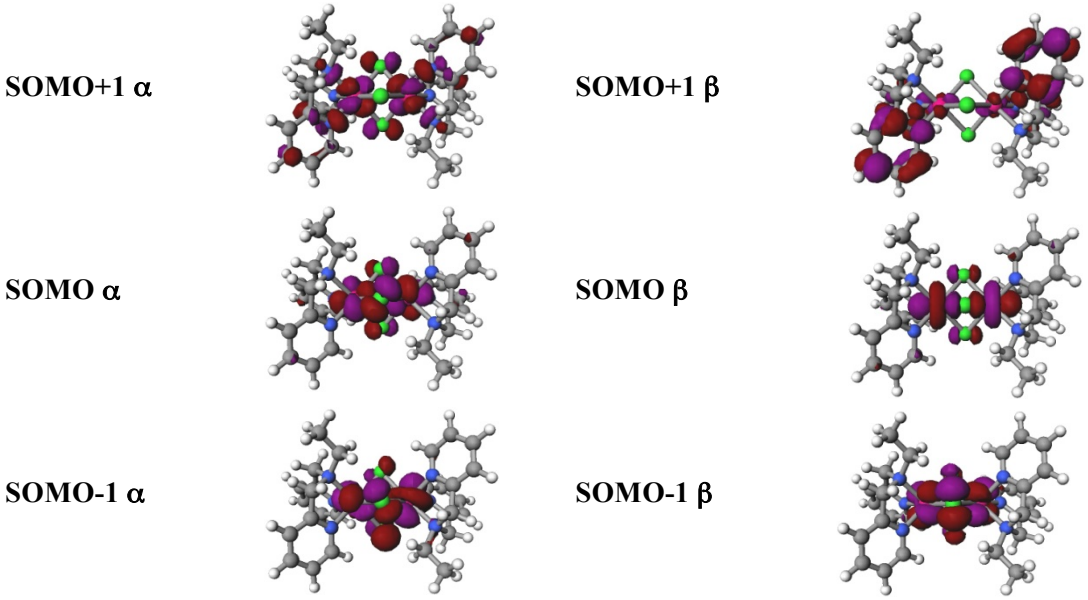

Fig. S13 Contributions to MOs from each atom of $[\mathbf{2}]^{2+}$

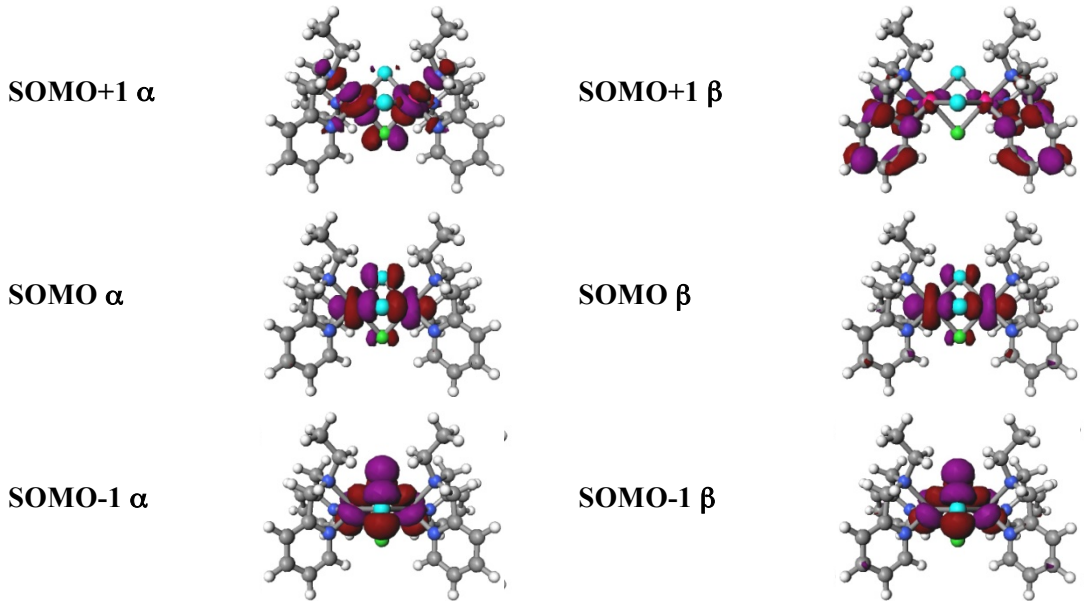

Fig. S14 Contributions to MOs from each atom of $[\mathbf{3}]^{2+}$